Advances in Engineering Innovation Vol.17 Issue 4 EWA Publishing
Available Online: 20 March 2026 DOI: 10.54254/2977-3903/2026.32335

Hyperspectral anomaly detection research fusing global and nonlocal low-rank factorization and nonconvex sparse constraints

Yujie Gao*[*]*, Jiayi Hu, Xiaomeng Hu

School of Mathematics, Southwest Minzu University, Chengdu, China

*Corresponding Author. Email: 2947749303@qq.com

Abstract. Hyperspectral anomaly detection is a key task in the field of remote sensing, which aims to identify targets with significant spectral differences from the background without prior knowledge. Traditional methods insufficiently characterize the sparsity of anomalies and are susceptible to background noise interference. This paper introduces the existing advanced low-rank denoising technique, Global and Nonlocal Low-Rank Factorization (GLF), for anomaly detection as a background modeling tool to obtain residual images. In the residual processing stage, a variety of nonconvex penalty functions are systematically adopted to replace the traditional L_2, and anomaly score maps are generated through pixel-wise aggregation to more accurately approximate the sparse distribution of anomalies. Experiments on multiple ABU datasets show that the AUC of the proposed GLF-NC is significantly superior to classical methods such as RX, RPCA-RX, and LRASR. Transferring GLF to anomaly detection combined with nonconvex penalties can effectively improve detection accuracy, verifying the effectiveness of the method in anomaly enhancement and background suppression.

Keywords: hyperspectral anomaly detection, Global and Nonlocal Low-Rank Factorization (GLF), nonconvex sparse constraints, low-rank representation

1. Introduction

Hyperspectral remote sensing technology acquires spectral information of ground objects in continuous narrow bands to form a "spectral cube" containing hundreds of bands, providing a unique data foundation for accurate ground object recognition. In this technical system, anomaly detection, as one of the core research directions, aims to identify targets with significant spectral differences from the background without prior knowledge, and has important application value in military reconnaissance, environmental monitoring, smart agriculture and other fields.

Existing hyperspectral anomaly detection methods can be mainly divided into three categories:

(1) Statistical methods. This type of method assumes that background pixels obey a certain statistical distribution, and realizes detection by calculating the deviation degree of the pixel to be tested from the background model. The classical RX detector [1] is based on the generalized likelihood ratio test, assumes that

the background obeys a multivariate Gaussian distribution, and calculates the Mahalanobis distance using the global mean and covariance matrix. Its advantages are simple calculation and strong real-time performance, but it has problems such as inaccurate statistical assumptions and anomaly contamination. Subsequent improvements include Local RX (LRX) [1], Kernel RX (KRX) [2] and Weighted RX (WRX) [3], which improve detection robustness by introducing local windows, kernel mapping or weighting strategies.

(2) Representation learning methods. This type of method utilizes the low-rank property of hyperspectral data and the sparsity of anomalies to decompose the image into background and anomaly components. Low-rank sparse decomposition models such as RPCA [4] and LRASR [5] are solved via convex optimization and achieve good separation effects.

(3) Deep learning methods. This type of method automatically extracts spatial and spectral features through end-to-end learning, significantly improving recognition accuracy. For example, Auto-Encoder (AE) [6] measures anomalies using reconstruction error, Generative Adversarial Network (GAN) [7] enhances anomaly detection capability through adversarial training, and Graph Neural Network [8] realizes detection based on the topological relationship between pixels. However, deep learning methods usually require massive training data and high computational costs, facing challenges when the sample size is limited.

Although low-rank sparse representation methods have achieved certain results, most of them adopt L_2 or L_1 as sparse constraints, which can hardly accurately fit the actual sparse distribution of anomaly targets. In recent years, nonconvex penalty functions have attracted much attention due to their excellent sparsity. For example, the GNBRL framework [9] proposes to adopt a class of nonconvex functions that constrain both low-rank property and sparsity by setting a theoretical error bound.

Global and Nonlocal Low-Rank Factorization (GLF) [10], as an advanced low-rank denoising method, fully mines the spatial-spectral correlation of hyperspectral images through global and nonlocal block matching, but its application in anomaly detection remains to be expanded.

Based on the above analysis, this paper proposes a hyperspectral anomaly detection method GLF-NC that combines GLF background modeling and nonconvex sparse constraints, thereby transferring GLF to the anomaly detection task. It uses its excellent noise removal and background estimation capabilities to obtain pure residuals, and introduces nonconvex penalties instead of the traditional L_2 to calculate anomaly scores, better approximating anomaly sparsity. The effectiveness of the proposed method is verified through experiments on multiple ABU datasets in comparison with various classical methods.

2. Research methods

2.1. GLF background modeling

Hyperspectral Image (HSI) is characterized by high correlation between bands and spatial self-similarity. Background pixels usually present a low-rank structure, while anomaly targets are sparsely distributed. Global and Nonlocal Low-Rank Factorization (GLF), proposed by Zhuang et al. [10], is a hyperspectral image denoising method based on global and nonlocal low-rank factorization. Its core principle is to remove noise by utilizing both global low-rank features and nonlocal self-similarity.

For the acquired raw hyperspectral image $X \in R^{H \times W \times B}$, where H, W and B denote the height, width and number of bands respectively, $X = X_0 + N$ is its noisy observation model, where $N \in R^{H \times W \times B}$ is additive noise. For the convenience of matrix operations, X is rewritten in matrix form as $X \in R^{B \times M}$, where the total number of pixels $M = H \times W$.

The optimization objective of this model is:

$$\widehat{Z} = arg\frac{1}{2}\left\|X - EZ\right\|_F^2 + \lambda\phi(Z) = arg\frac{1}{2}\left\|E^TX - Z\right\|_F^2 + \lambda\phi(Z), \tag{1}$$

where the background is approximated as a low-dimensional subspace $X_0 = EZ$, the subspace basis $E \in R^{B\times k}$, $Z \in R^{k\times M}(k \ll B)$ is the low-dimensional representation coefficient image, $\|\cdot\|_F$ is the Frobenius norm, $\phi(\cdot)$ reflects nonlocal self-similarity, and λ is the regularization parameter. On the low-dimensional representation coefficient Z , this model divides the image into overlapping 3D patches (each patch contains a spatial neighborhood and all bands), globally searches for similar patches to form clusters, and imposes low-rank constraints on each cluster, thereby effectively separating the background from noise to obtain the denoised coefficient $\widehat{Z}$ and the denoised image $\widehat{X_0} = E\widehat{Z}$.

Based on the idea of GLF, this paper remodels it as a background estimation algorithm for anomaly detection, changing from recovering noise-free images to fitting low-rank backgrounds, where Z_{bg} is the low-dimensional representation coefficient containing only background information, and the background image $B = E\widehat{Z_{bg}}$.

2.2. Residual generation and representation

The residual image is defined as:

$$R = X - B, \tag{2}$$

the residual R contains all information not covered by the background model. The residual is converted into a two-dimensional matrix form $\widetilde{R} \in R^{B\times N}$, where $N = H \times W$ represents the total number of pixels. For each pixel p , its residual vector $r_p = [r_{p,1}, r_{p,2}, \ldots, r_{p,B}]^T \in R^B$. The task of hyperspectral anomaly detection can be rephrased as constructing a mapping function from residual vectors to anomaly scalar values, so that anomaly pixels obtain values significantly higher than background pixels.

2.3. Nonconvex sparse constraint functions

Traditional methods often use L_2 to calculate anomaly values:

$$s_p^{L_2} = \|r_p\|_2 = \sqrt{\textstyle\sum_{b=1}^{B} r_{p,b}^2}, \tag{3}$$

however, L_2 is a convex function, and its square property makes it sensitive to small-amplitude noise and cannot effectively approximate the L_0 sparsity. To overcome this limitation, this paper introduces the following three nonconvex penalty functions [9]:

(1) LogSum Penalty:

$$s_p^{Log} = \textstyle\sum_{b=1}^{B} log(1 + \frac{|r_{p,b}|}{\varepsilon}), \tag{4}$$

where $\varepsilon > 0$ is the smoothing parameter, set to 10^{-6} in this paper. As a smooth approximation of the L_0, this function has the ability to adaptively retain large-amplitude anomalies.

(2) L_p Penalty $(0 < p < 1)$:

$$s_p^{Lp} = \textstyle\sum_{b=1}^{B} |r_{p,b}|^p, \tag{5}$$

$p = 0.5$ is adopted in this paper. The L_p penalty has an infinite slope near zero, imposes heavy penalties on small-amplitude noise, and can better reflect sparsity.

(3) Minimax Concave Penalty (MCP):

$$s_p^{MCP} = \textstyle\sum_{b=1}^{B} \rho(r_{p,b}; \alpha), \tag{6}$$

where $\rho(x;\alpha)=\begin{cases}|x|-\frac{x^2}{2\alpha}, & |x|\le\alpha\\ \frac{\alpha}{2}, & |x|>\alpha\end{cases}$, $\alpha=1.0$ is adopted in this paper. MCP has excellent statistical properties such as unbiasedness, continuity and sparsity.

This paper compares the performance of the above penalty functions through experiments. Since the background is fixed by GLF, anomaly scoring only involves pixel-wise closed-form computation without iterative optimization, thus featuring high computational efficiency.

2.4. Anomaly detection fusing GLF and nonconvex sparse constraints

In summary, the proposed anomaly detection model fusing GLF and nonconvex sparse constraints (GLF-NC) is:

$$S=Reshape([\textstyle\sum_{b=1}^{B}\rho((X-E\widehat{Z_{bg}})_{jb};\alpha)]_{j=1}^{N},[H,W]),\tag{7}$$

$E\widehat{Z_{bg}}$ denotes the optimal low-rank background solved by the GLF algorithm, $\widehat{Z_{bg}}$ is the optimal coefficient matrix of GLF, and the spectral residual of the j -th pixel in the b -th band is $(X-E\widehat{Z_{bg}})_{jb}$. The nonconvex function $\rho(\cdot;\alpha)$ is applied to it to realize anomaly recognition. $S=Reshape(s,[H,W])$, where $Reshape(\cdot)$ denotes the dimension reshaping operation in image processing, mapping the 1D anomaly score vector s to a 2D anomaly map of size $H\times W$, consistent with the built-in function reshape() in MATLAB.

This model is solved using a two-stage decoupled algorithm: the first stage uses GLF for background estimation, and the second stage applies nonconvex sparse penalties to the residual to calculate anomaly values. The complete process is shown in Table 1.

Table 1. Anomaly detection algorithm fusing GLF and nonconvex sparse constraints

```
Input: Hyperspectral image $X\in R^{H\times W\times B}$, subspace dimension $k$, nonconvex function type and related parameters
Output: Anomaly map $S\in R^{H\times W}$
1. Estimate the background $B$ using GLF
2. Calculate the residual $R=X-B$
3. Convert the residual into a two-dimensional matrix form $\widetilde{R}\in R^{B\times N}$, where $N=H\times W$
4. for each pixel $j=1$ to $N$ do
5.     $r_j=\widetilde{R}(:,j)$ % Residual vector corresponding to the $j$-th pixel
6.     Calculate the anomaly value $s_j$ according to the selected nonconvex function
7. end for
8. Convert the anomaly value vector $s=[s_1,s_2,\dots,s_N]$ into an image $S$
9. Return the anomaly map $S$
```

3. Experiment and result analysis

3.1. Data description

Three public datasets, abu-beach-2, abu-urban-3 and abu-airport-4, are selected in the experiment to detect hyperspectral anomalies. These datasets cover three typical surface scenes: coastal area, urban area and airport area, which can effectively verify the reliability of the algorithm in diverse environments. For all datasets, the actual positions of anomaly targets are manually annotated on the map.

(1) abu-beach-2 dataset: Collected by a hyperspectral sensor, it is a coastal zone/marine scene with a spatial resolution of 100×100 pixels and 102 spectral bands. Anomaly targets refer to sailing ships or small man-made objects.

(2) abu-urban-3 dataset: Collected in an urban area, the image has a spatial size of 100×100 pixels and 205 spectral bands. The scene contains buildings, roads, vegetation and shadows, and anomaly targets are mainly vehicles and roofs.

(3) abu-airport-4 dataset: It presents an airport scene with a spatial size of 100×100 pixels and 205 spectral bands. The scene includes aprons, runways, buildings and vegetation, and aircraft on the apron are anomaly targets.

In the experiment, the Receiver Operating Characteristic (ROC) curve and the Area Under the Curve (AUC) are used as the main evaluation metrics. Compared with the single-threshold accuracy metric, the ROC curve can comprehensively reflect the target recognition capability of the algorithm at different false alarm levels. As a threshold-independent comprehensive metric, AUC is suitable for comparing the overall performance of different algorithms.

Figure 1 shows the pseudo-color images and the corresponding ground truth anomaly target maps of the three datasets.

(a) Pseudo-color image of abu-beach-2 (b) Pseudo-color image of abu-urban-3 (c) Pseudo-color image of abu-airport-4

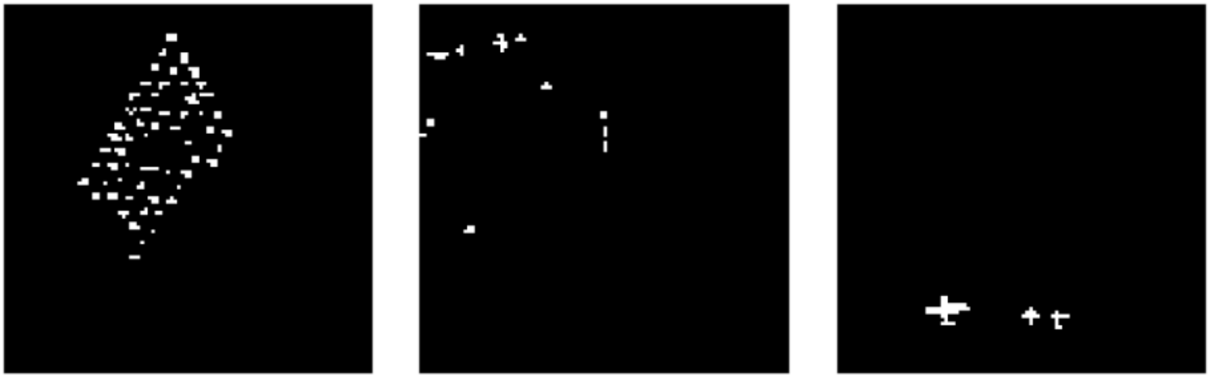

(d) Ground truth anomaly target map of abu-beach-2 (e) Ground truth anomaly target map of abu-urban-3 (f) Ground truth anomaly target map of abu-airport-4

Figure 1. Pseudo-color images and corresponding ground truth anomaly target maps of the three datasets

3.2. Comparative experimental results

To evaluate the effectiveness of the proposed method, five classical anomaly detection algorithms are selected for comparison: RX [1], RPCA-RX [4], LSMAD [11], LSDM-MoG [12] and LRASR [5]. The detection results of the proposed algorithm using the LogSum nonconvex function and the optimal subspace dimension obtained by parameter scanning on the abu-beach-2 dataset are shown in Figure 2.

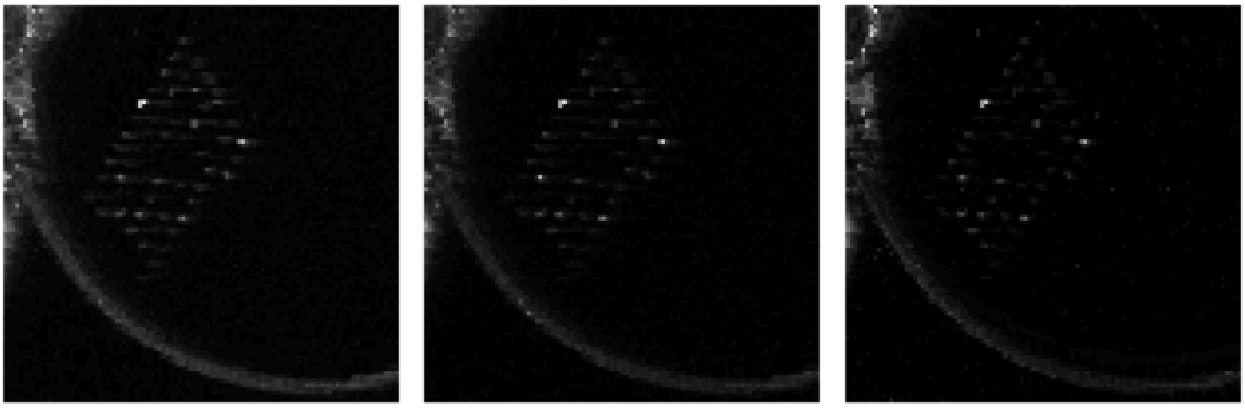

(a)RX (b)RPCA-RX (c)LSMAD

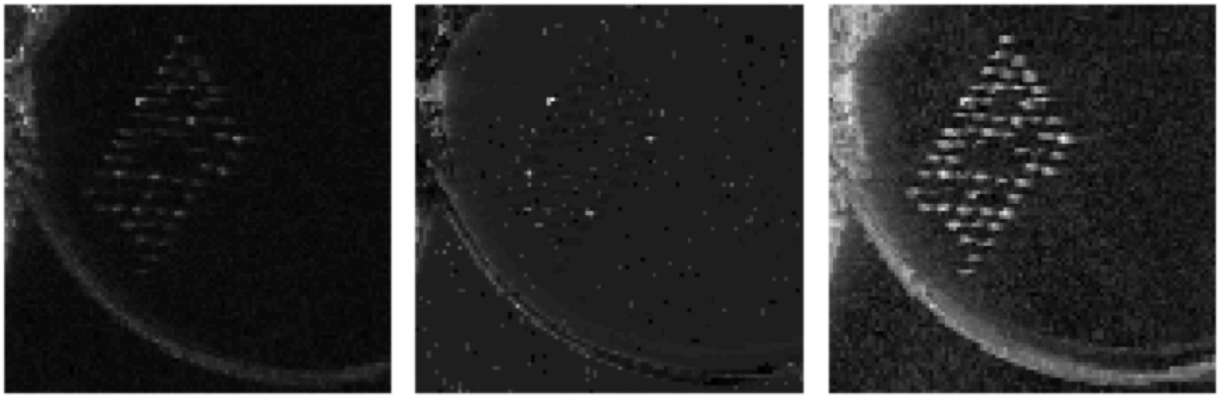

(d)LSDM-MoG (e)LRASR (f)GLF-NC

Figure 2. Detection result maps of 6 algorithms on the abu-beach-2 dataset

Figure 2 intuitively presents the detection result maps on the abu-beach-2 dataset. It can be seen that the anomaly targets detected by GLF-NC are more comprehensive, while the detection results of other algorithms have many omissions. The ROC curve can comprehensively reflect the detection capability of the algorithm at different false alarm levels; the stronger the detection capability of the algorithm, the closer the curve is to the upper left corner. The ROC curve on the abu-beach-2 dataset is shown in Figure 3(a). The ROC curve of GLF-NC is closer to the upper left corner than those of other algorithms.

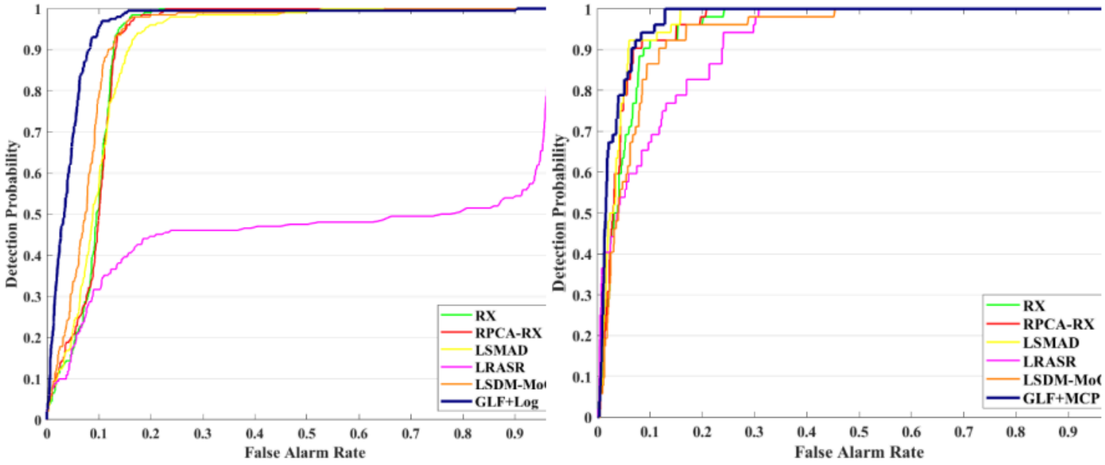

|(a) ROC curve on the abu-beach-2 dataset (b) ROC curve on the abu-urban-3 dataset|

Figure 3. ROC curves of 6 algorithms on the abu-beach-2 and abu-urban-3 datasets respectively

(a)RX (b)RPCA-RX (c)LSMAD

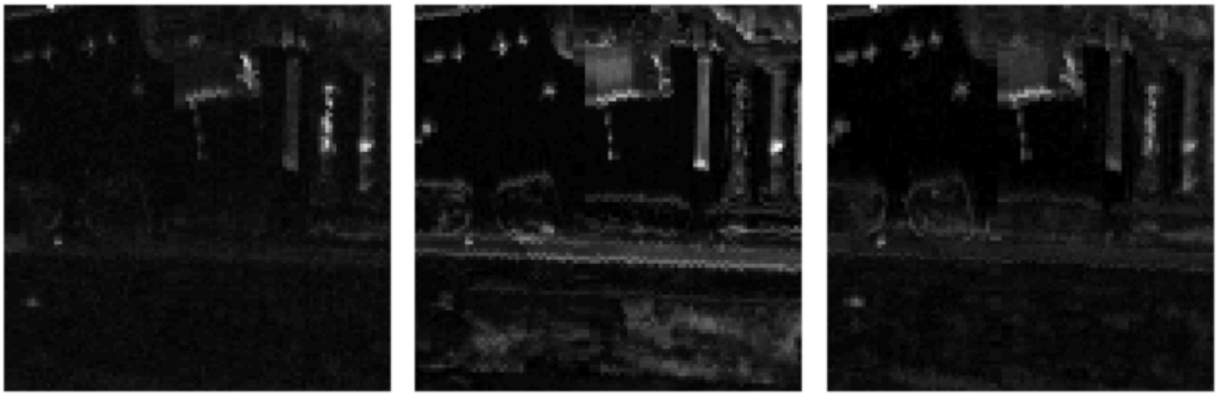

(d)LSDM-MoG (e)LRASR (f)GLF-NC

Figure 4. Detection result maps of 6 algorithms on the abu-urban-3 dataset

Figure 4 shows the anomaly detection result maps of 6 algorithms on the abu-urban-3 dataset. Here, the proposed algorithm adopts the MCP nonconvex function and the optimal subspace dimension obtained by parameter scanning. It can be seen from the figure that the anomaly targets detected by GLF-NC are relatively complete with a relatively low false detection rate, while the anomaly targets detected by the other 5 algorithms are not obvious. The ROC curve of the abu-urban-3 dataset is shown in Figure 3(b). Compared with other algorithms, the ROC curve of GLF-NC is closer to the upper left corner, indicating better detection performance.

AUC provides a threshold-independent comprehensive metric suitable for comparing the overall performance of different algorithms. The closer its value is to 1, the better the overall performance of the algorithm. The AUC values of 6 algorithms on the three datasets are shown in Table 2 below. From the AUC results of the three datasets, the GLF-NC algorithm achieves the highest AUC values in all scenarios in this paper, which are 0.9574, 0.9712 and 0.9939 respectively, showing the strongest comprehensive detection capability and significantly outperforming other comparison algorithms.

Table 2. AUC comparison of different algorithms on different datasets

DataSet	abu-beach-2	abu-urban-3	abu-airport-4
RX	0.9106	0.9513	0.9526
RPCA-RX	0.9097	0.9577	0.9627
LSMAD	0.9041	0.9636	0.9865
LSDM-MoG	0.9244	0.9375	0.9303
LRASR	0.4687	0.9187	0.9462
GLF-NC	0.9574	0.9712	0.9939

To verify the effectiveness of nonconvex sparse constraints, this paper compares the detection performance of three nonconvex penalties with the traditional L_2 on the abu-airport-4 dataset under the condition of the optimal subspace dimension $k = 12$ selected according to experimental performance. The experimental results are shown in Figure 5.

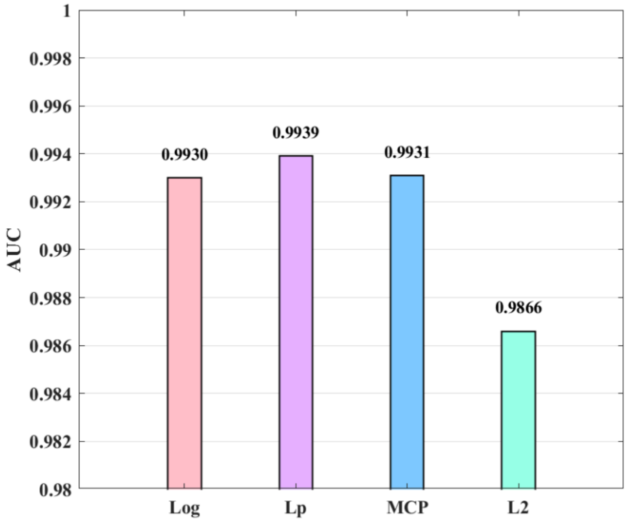

Figure 5. Detection performance of nonconvex penalties and the traditional L_2

It can be seen from Figure 5 that the AUC values of the three nonconvex penalties are very close, but all are significantly higher than that of L_2. This result indicates that nonconvex functions can more accurately approximate the ideal L_0 sparsity, thereby enhancing anomaly signals and suppressing background noise more effectively.

3.3. Subspace dimension analysis

The subspace dimension k in GLF background modeling is one of the key parameters affecting detection performance. To analyze its influence, taking the LogSum function as an example, this paper tests the AUC values when $k \in \{5, 8, 10, 12, 15, 20\}$ on the abu-airport-4 dataset, and the results are shown in Figure 6. It can be seen from the figure that the AUC first increases and then slightly decreases with the increase of k : when k is too small, the low-rank approximation of the background is too rough, and more background information remains in the residual, leading to an increase in the false alarm rate; when k is too large, some anomalies may be over-fitted into the background model, weakening the anomaly response. The optimal k value varies slightly across different datasets. For the abu-airport-4 dataset in this experiment, the optimal $k = 12$, at which the AUC value reaches 0.9930.

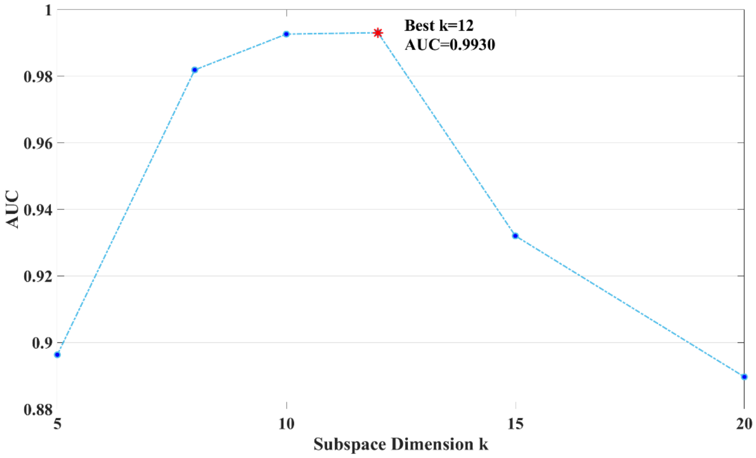

Figure 6. k-AUC curve of GLF-LogSum on the abu-airport-4 dataset

4. Conclusion

This paper proposes a hyperspectral anomaly detection method fusing global and nonlocal low-rank factorization and nonconvex sparse constraints. This method first uses GLF background modeling to fully mine the spatial-spectral correlation of hyperspectral images, so as to estimate the background more accurately and obtain a pure residual image. On this basis, a family of nonconvex penalty functions including LogSum, L_p and MCP is introduced to replace the traditional L_2 for sparse constraints on the residual, effectively solving the problems of insufficient characterization of anomaly sparsity and susceptibility to background noise interference of the traditional L_2, and enabling more accurate enhancement of anomaly signals and suppression of background clutter. Experimental results show that nonconvex penalties can effectively improve detection accuracy, and GLF-NC outperforms various classical methods in AUC values on the abu-beach-2, abu-urban-3 and abu-airport-4 datasets. Future work will further explore adaptive parameter selection and the application of more nonconvex functions in hyperspectral anomaly detection.

Funding project

Supported by the College Students' Innovation and Entrepreneurship Training Program of Southwest Minzu University (Grant No. 202510656007).

References

[1] Reed, I. S., & Yu, X. (1990). Adaptive multiple-band CFAR detection of an optical pattern with unknown spectral distribution. *IEEE Transactions on Acoustics, Speech, and Signal Processing, 38*(10), 1760–1770. https: //doi.org/10.1109/29.60100

[2] Kwon, H., & Nasrabadi, N. M. (2005). Kernel RX-algorithm: A nonlinear anomaly detector for hyperspectral imagery. *IEEE Transactions on Geoscience and Remote Sensing, 43*(2), 388–397. https: //doi.org/10.1109/TGRS.2004.841487

[3] Guo, Q., Zhang, B., Ran, Q., Gao, L., Li, J., & Plaza, A. (2014). Weighted-RXD: A novel approach for anomaly detection in hyperspectral imagery. *IEEE Journal of Selected Topics in Applied Earth Observations and Remote Sensing, 7*(6), 2414–2425. https: //doi.org/10.1109/JSTARS.2014.2310753

[4] Candès, E. J., Li, X., Ma, Y., & Wright, J. (2011). Robust principal component analysis? *Journal of the ACM, 58*(3), 1–37. https: //doi.org/10.1145/1970392.1970395

[5] Xu, Y., Wu, Z., Li, J., Plaza, A., & Wei, Z. (2016). Anomaly detection in hyperspectral images based on low-rank and sparse representation. *IEEE Transactions on Geoscience and Remote Sensing, 54*(4), 1990–2000. https: //doi.org/10.1109/TGRS.2015.2493201

[6] Bati, E., Caliskan, A., Koz, A., & Alatan, A. A. (2015). Hyperspectral anomaly detection method based on auto-encoder. In *Proceedings of SPIE Remote Sensing* (Vol. 9643, Article 96430N). SPIE. https: //doi.org/10.1117/12.2194816

[7] Arisoy, S., Nasrabadi, N. M., & Kayabol, K. (2020). GAN-based hyperspectral anomaly detection. In *Proceedings of the 28th European Signal Processing Conference* (EUSIPCO 2020) (pp. 1547–1551). IEEE. https: //doi.org/10.23919/Eusipco47968.2020.9287675

[8] R, A., Gao, Q., Zhang, X., Feng, W., & Ali, S. K. (2025). Hyperspectral anomaly detection leveraging spatial attention and right-shifted spectral energy. *PLoS ONE, 20*(9), Article e0330640. https: //doi.org/10.1371/journal.pone.0330640

[9] Yu, Q., & Bai, M. (2024). Generalized nonconvex hyperspectral anomaly detection via background representation learning with dictionary constraint. *SIAM Journal on Imaging Sciences, 17*(2), 917–950. https: //doi.org/10.1137/23M158902X

[10] Zhuang, L., Fu, X., Ng, M. K., & Bioucas-Dias, J. M. (2021). Hyperspectral image denoising based on global and nonlocal low-rank factorizations. *IEEE Transactions on Geoscience and Remote Sensing, 59*(12), 10438–10454. https: //doi.org/10.1109/TGRS.2020.3046038

[11] Zhang, Y., Du, B., Zhang, L., & Wang, S. (2017). Low-rank and sparse decomposition for hyperspectral anomaly detection. *IEEE Journal of Selected Topics in Applied Earth Observations and Remote Sensing, 10*(4), 1536–1548. https: //doi.org/10.1109/JSTARS.2016.2638728

[12] Li, L., Li, W., Du, Q., & Tao, R. (2021). Low-rank and sparse decomposition with mixture of Gaussian for hyperspectral anomaly detection. *IEEE Transactions on Cybernetics, 51*(9), 4369–4382. https: //doi.org/10.1109/TCYB.2020.2968750